Impermeable inorganic “walls” sandwiching perovskite layer toward inverted and indoor photovoltaic devices

Xu, Jie; Xi, Jun; Dong, Hua; Ahn, Namyoung; Zhu, Zonglong; Chen, Jinbo; Li, Peizhou; Zhu, Xinyi; Dai, Jinfei; Hu, Ziyang

Published in:
Nano energy

DOI:
10.1016/j.nanoen.2021.106286

Publication date:
2021

Nano Energy 88 (2021) 106286

Contents lists available at ScienceDirect

Nano Energy

journal homepage: www.elsevier.com/locate/nanoen

Impermeable inorganic "walls" sandwiching perovskite layer toward inverted and indoor photovoltaic devices

Jie Xu [a,1], Jun Xi [b,*,1], Hua Dong [a,g,**], Namyoung Ahn [d], Zonglong Zhu [e], Jinbo Chen [a], Peizhou Li [a], Xinyi Zhu [a], Jinfei Dai [a], Ziyang Hu [f], Bo Jiao [a], Xun Hou [a], Jingrui Li [c,*], Zhaoxin Wu [a,g,**]

[a] Key Laboratory for Physical Electronics and Devices of the Ministry of Education & Shaanxi Key Lab of Information Photonic Technique, School of Electronic Science and Engineering, Xi'an Jiaotong University, No. 28, Xianning West Road, Xi'an 710049, China
[b] Zernike Institute for Advanced Materials, University of Groningen, Nijenborgh 4, 9747 AG Groningen, the Netherlands
[c] Electronic Materials Research Laboratory, Key Laboratory of the Ministry of Education & International Center for Dielectric Research, School of Electronic Science and Engineering, Xi'an Jiaotong University, Xi'an 710049, China
[d] Chemistry Division, Los Alamos National Laboratory, Los Alamos, NM 87545, USA
[e] Department of Chemistry, City University of Hong Kong, Kowloon, Hong Kong
[f] Department of Microelectronic Science and Engineering, Ningbo University, Ningbo 315211, China
[g] Collaborative Innovation Center of Extreme Optics, Shanxi University, Taiyuan 030006, China

ARTICLE INFO

Keywords:
Perovskite solar cells
Alkali fluorides
Interface recombination
Stability
Indoor photovoltaics

ABSTRACT

Interfaces between the perovskite active layer and the charge-transport layers (CTLs) play a critical role in both efficiency and stability of halide-perovskite photovoltaics. One of the major concerns is that surface defects of perovskite could cause detrimental nonradiative recombination and material degradation. In this work, we addressed this challenging problem by inserting ultrathin alkali-fluoride (AF) films between the tri-cation lead-iodide perovskite layer and both CTLs. This bilateral inorganic "walls" strategy makes use of both physical-blocking and chemical-anchoring functionalities of the continuous, uniform and compact AF framework: on the one hand, the uniformly distributed alkali-iodine coordination at the perovskite-AF interfaces effectively suppresses the formation of iodine-vacancy defects at the surfaces, thus reducing the trap-assisted recombination at the perovskite-CTL interfaces and therewith the open-voltage loss; on the other hand, the impermeable AF buffer layers effectively prevent the bidirectional ion migration at the perovskite-CTLs interfaces even under harsh working conditions. As a result, a power-conversion efficiency (PCE) of 22.02% (certified efficiency 20.4%) with low open-voltage deficit (<0.4 V) was achieved for the low-temperature processed inverted planar perovskite solar cells. Exceptional operational stability (500 h, ISOS-L-2) and thermal stability (1000 h, ISOS-D-2) were obtained. Meanwhile, a 35.7% PCE was obtained under dim-light source (1000 lux white LED light) with the optimized device, which is among the best records in perovskite indoor photovoltaics.

1. Introduction

In recent years, people have witnessed an astonishing progress of organic-inorganic hybrid perovskite optoelectronic devices thanks to their excellent electronic, optical, and charge-transport properties [1–7]. Currently, the power conversion efficiency (PCE) of perovskite solar cells (PSCs) and perovskite indoor-photovoltaic devices have reached 25.5% and 36%, respectively, rivaling the traditional silicon- and GaAs-based devices [8,9]. Nevertheless, there is still a long way to go for approaching the Shockley-Queisser theoretical limit (34% under AM 1.5 G solar spectrum) of single-junction devices [10]. So far, a majority of achievements that simultaneously realized high efficiency and high stability are based on the n-i-p (normal) device structure, for which the thick hole-transport layer (HTL) with chemical doping leads to high

* Corresponding authors.
* Corresponding author at: Key Laboratory for Physical Electronics and Devices of the Ministry of Education & Shaanxi Key Lab of Information Photonic Technique, School of Electronic Science and Engineering, Xi'an Jiaotong University, No. 28, Xianning West Road, Xi'an 710049, China.
E-mail addresses: j.xi@rug.nl (J. Xi), donghuaxjtu@mail.xjtu.edu.cn (H. Dong), jingrui.li@mail.xjtu.edu.cn (J. Li), zhaoxinwu@mail.xjtu.edu.cn (Z. Wu).
[1] These two authors contributed equally to this work.

https://doi.org/10.1016/j.nanoen.2021.106286
Received 31 March 2021; Received in revised form 24 May 2021; Accepted 21 June 2021
Available online 24 June 2021

fabrication cost and inevitable stability risk. In contrast, PSCs of inverted (p-i-n) planar structure with low processing temperature and thinner, undoped HTL are considered promising for industrial production of versatile devices ranging from standard single-junction cells to flexible and tandem cells [11–15]. The latest record of inverted-structure PSC's PCE is 23.37% [12].

Unfortunately, inverted-structure PSCs still lag behind the n-i-p counterparts in terms of both efficiency and stability. Nonradiative recombination induced by defects in the bulk phase of material and at the surfaces and grain boundaries is one of the main factors that limits the device performance [11,16]. While bulk defects can be properly controlled by means of several mature methodologies [17–21], suppressing the formation of defects at the perovskite surfaces remains a major challenge in today's perovskite optoelectronic community [11,16]. Specifically, these defects especially iodine-vacancy (v_I) induce trap states within the bandgap of the perovskite semiconductor, which facilitate nonradiative recombination at the interfaces thus giving rise to open-circuit voltage (V_{OC}) loss and therewith limited PCE [12]. In addition, the device stability could be strongly affected by the trapped charges at the interfaces between the perovskite layer and CTLs upon the defect formation, as the thus-induced electric field would initiate and accelerate the decomposition of perovskite and deprotonation of the organic moieties [22,23].

A variety of methods have been developed to mediate the interfacial problem, which can be classified into the organic and the inorganic strategies. Amine-group-containing large organic ligands with a favorable diversity of candidate molecules have proven to be effective in passivating the perovskite surfaces [12,24–26]. However, the regular orientation of long-chain or bulky organic molecules is hard to achieve on a length scale beyond a few lattice constants of perovskite. Hence, steric hindrance within the organic-ligand layer is prevailing and problematic, as it induces the distortion of perovskite lattices at the surface as well as the decay and incomplete coverage of the organic layer, which eventually leads to the instability of materials and devices in long-term applications under harsh working conditions. Although polymer strategy shows great potential for inhibiting humidity, two major challenges still remain, as follows. (i) By far, polymer strategies are mainly implemented by physical blending. Due to the poor compatibility between polymer and ionic perovskite, inhomogeneous and microvoid-containing morphology of polymer/perovskite film will be formed in the PSCs. As a result, the phase separation between polymer and host material may deteriorate the device efficiency and stability. (ii) The device performance is extremely sensitive to the incorporated polymer concentration or thickness due to the low charge mobility or the electrical insulation of available polymers. This may not be compatible with the robust process requirements for large-area manufacture [27–30]. The inorganic strategy is also reported benefiting from its own stability. It was reported that incorporating Li^+, Na^+, K^+, and Rb^+ into the perovskite lattice can significantly reduce the nonradiative recombination thus improving the efficiency and stability [31–35]. However, how to guarantee that the doping takes effect uniformly and completely at the perovskite surfaces and grain boundaries remains a problem. In addition, further surface passivation (such as via introducing organic ligands) might be required, as the surfaces of the doped perovskite is not yet physically well-protect against interfacial ion diffusion and possible contact with environmental small molecules such as oxygen and water. In parallel, inorganic buffer-layer technologies are also employed to inhibit the improper ion diffusion [36,37]. It is required that the interaction between the buffer layer and the perovskite can anchor the surface atoms of the latter without inducing a large perovskite-lattice distortion. The choice of inorganic materials is important, however, corresponding discussion about the choice of inorganic materials is still rare. Thus an inorganic protocol designed to simultaneously minimize the defects and block the ion diffusion over the interfaces between the perovskite layer and both CTLs in the inverted planar devices is highly appealed.

In this work, we developed an inorganic bilateral strategy to engineer the surfaces of the tri-cation lead-iodide perovskite layer in the inverted planar structure of PSC. Ultrathin alkali-halide buffer layers were facilely inserted between the perovskite layer and both the electron-transport layer (ETL) and the HTL. Considering F's smallest anionic radius and therewith the most stable and compact alkali-fluoride (AF) frameworks, we used fluorides with different alkali cations as buffer-layer materials in this work, namely lithium fluoride (LiF), sodium fluoride (NaF), and potassium fluoride (KF). Benefiting from the chemical-anchoring functionality, the uniformly distributed alkali-iodide coordination between the buffer layer and perovskite could effectively passivate the surface defects without affecting the perovskite lattice. Moreover, the bilateral protection could physically prevent the bidirectional ion migration and oxygen or moisture invasion to the perovskite due to AF's compact and stable features. With this facile bilateral inorganic "walls" strategy, we achieved a PCE of 22.02% for a KF-modified inverted planar solar cell, which allows an exceptional operating stability (500 h, ISOS-L-2) and thermal stability (1000 h, ISOS-D-2). Interestingly, the optimized bilaterally-modified device also exhibited a remarkable performance under dim-light condition, which achieved a 35.7% efficiency under 1000 lux white LED light. We expect this work can provide an inorganic perspective to effectively manage the trap-assisted defects and facilitate long-term stable and highly efficient perovskite optoelectronic devices toward industrial production.

2. Results and discussion

The inverted planar perovskite-based device with bilateral AF modification (denoted by AF-perovskite-AF hereafter) is sketched in Fig. 1a. The traditional one-step antisolvent method was adopted to prepare the perovskite thin film with optimized component $Cs_{0.05}(FA_{0.88}MA_{0.12})_{0.95}PbI_3$ on the substrate (details given in Experimental Section). The cross-sectional scanning electron microscopy (SEM) image in Fig. 1b shows a perfect planar device structure, which comprises stacked layers of indium tin oxide (ITO, 130 nm)/poly[bis(4-phenyl)(2,4,6-trimethylphenyl)amine] (PTAA, 8 nm)/perovskite (500 nm)/C_{60} (30 nm)/bathocuproine (BCP, 6 nm) / Ag (120 nm). Notably, the bilateral AF buffer layers are too thin (<5 nm) to observe.

The dependence of device performance on respective AF thickness is summarized in Table S1. For A = Li, Na, or K, the device efficiency was maximized with the thickness of both buffer layers equal to 3 nm. The statistical distributions of PCE and V_{OC} from 120 devices with or without modification are shown in Fig. 1c and d, respectively. The representative PCE for the control (i.e., without bilateral AF modification), LiF-perovskite-LiF, NaF-perovskite-NaF, and KF-perovskite-KF devices are 18.45%, 19.76%, 20.22%, and 21.29%, respectively. This finding indicates that the bilateral AF "walls" significantly improve the photovoltaic performance of devices, and exhibits the trend of increasing PCE from LiF, NaF to KF. This is mainly contributed by the significant enhancement of V_{OC} (from 1.06 V for the control to 1.15 V for the KF-perovskite-KF device), while other metrics were also slightly improved (Fig. S1). Fig. 1e gives the current density – voltage (*J-V*) curves of the best-performing control and KF-perovskite-KF devices. The performance parameters of control are PCE = 19.20%, short circuit current density (J_{SC}) = 22.56 mA/cm^2, V_{OC} = 1.067 V, and fill factor (FF) = 79.80%; while the KF-perovskite-KF device achieves a largely improved PCE of 22.02% with J_{SC} = 23.40 mA/cm^2, V_{OC} = 1.152 V, and FF = 81.70%. The parameters of other two AF-modified devices are given in Table S2 and Fig. S2a. To the best of our knowledge, we have achieved the highest efficiency of inverted planar devices with a simple buffer-layer technology (detailed reference data given in Table S3). We here choose to assess the influence of masking. The most pronounced feature in Fig. S2b is instead the clear impact of smaller masks on both V_{OC} and FF. To confirm our in-laboratory device efficiency measurements, external certification of our nonencapsulated devices by the National Institute of Metrology, China, shows a PCE of 20.4% (V_{OC} = 1.094 V, J_{SC}

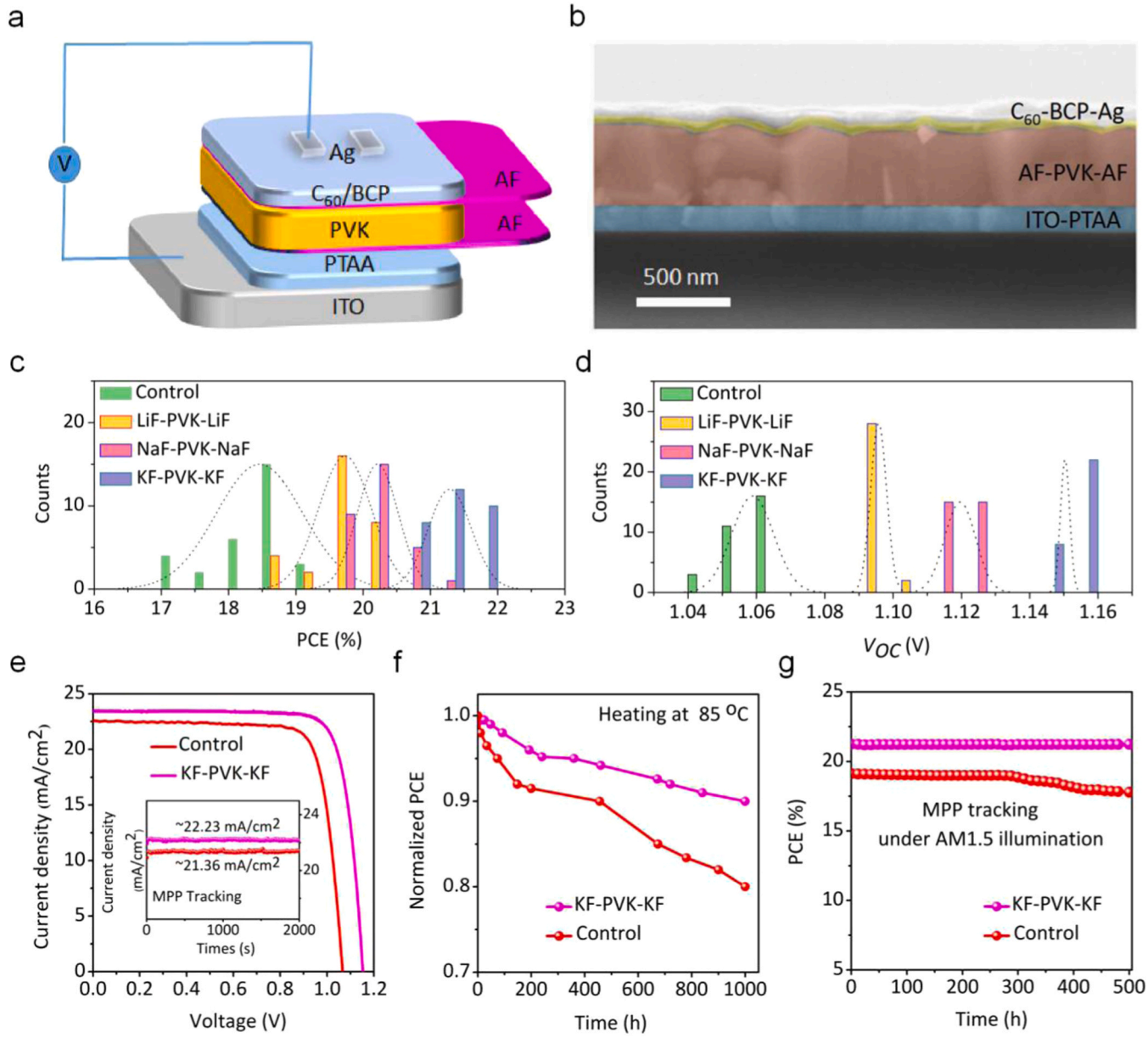

Fig. 1. Device performance. (a) Schematic illustration of the PSCs device structure. (b) Cross-sectional SEM image of the actual device with different layers indicated by false-coloring (scale bar: 500 nm). (c) Statistical distribution of PCE for 120 devices (30 per structure). (d) Statistical distribution of V_{OC} for 120 devices (30 per structure). (e) *J-V* curves of champion devices (inset: stabilized photocurrent output at the maximum power point). Stabilities of the control and the bilateral KF-modified PSCs: (f) thermal stability by putting the PSCs at 85 °C hot plate in N_2 for 1000 h, and (g) operational stability of PSCs under continuous illumination in N_2 for 500 h. PVK stands for perovskite in the figures of this manuscript.

= 23.22 mA/cm^2, and FF = 80.2%) as given in Fig. S3. Meanwhile, the steady-state photocurrents of the best-performing devices at maximum power point tracking (inset of Fig. 1e) are in good agreement with the *J-V* scanning results, thus supporting the reliability of the highest efficiency. As shown in Fig. S4, the integrated short-circuit current densities from the incident photon-to-electron conversion efficiencies (IPCE) are consistent with the J_{SC} from *J-V* measurement, thus validating the measured device performance. Fig. S5a shows the representative *J-V* curves of the KF-perovskite-KF device and the control device under the reverse and forward scan, whose performance parameters are listed in Table S4. Using hysteresis index (HI) which is defined by HI = [PCE (reverse) - PCE(forward)]/PCE (forward) to characterize the hysteresis, Table S4 indicates that the bilateral strategy with KF has largely reduced the HI from 3.3% to 0.3%, thus signifying perfectly balanced charge carrier extraction. For the KF-perovskite-KF device with 1 cm^2 solar cells, Fig. S5b shows a PCE of 19.65% with negligible hysteresis. In addition, the optimal characteristic parameters of unilateral strategy with different KF thickness are added in Table S5, including ITO-PTAA-KF-Perovskite-C_{60}-BCP-Ag, and ITO-PTAA-Perovskite-KF-C_{60}-BCP-Ag two structures. Although unilateral modification also improves the device efficiency, the effect is not as significant as that of bilateral strategy with KF.

To characterize the stability improvement upon the bilateral KF-modification, we conducted a series of measurements on unencapsulated devices. The results of stability tested at 85 °C in a nitrogen atmosphere (ISOS-D-2) and under continuous one-sun illumination (ISOS-L-2) are shown in Fig. 1f and g, respectively. From Fig. 1f, the introduction of bilateral KF ultrathin buffer layers has significantly improved the thermal stability of devices, as they retain 90% of the initial PCE after 1000 h, while the control ones retain only 80%. Fig. 1g indicates

the outstanding light-stability of the KF-perovskite-KF devices as they retain 100% of the original PCE after being exposed to one-sun illumination for 500 h. Finally, we also added the surrounding environment stability in Fig. S6 , the bilateral modification showed better environmental stability than unilateral modification.

To understand the underlying physics of the performance improvement of the inverted planar PSCs upon the incorporation of bilateral AF (in particular KF) thin films into the device, we first characterize the related materials properties in this section, then analyze the mechanism of charge properties and processes in the next sections.

Fig. 2a shows the morphology of the control and the KF-modified perovskite films. The blurred image in Fig. 2a-right vividly shows that the continuous, ultrathin and transparent KF buffer layer almost completely covers the perovskite. One can observe that the KF modification results in a slightly larger grain size, which is possibly because the interaction with KF subtly mediates the surface tension of perovskite so as to affect the dynamics of nucleation [38]. Similar morphological features can be observed from the other films modified by the bilateral LiF and NaF (Fig. S7). The profile elemental (alkali elements and fluorine) mapping (Fig. S8) from the energy-dispersive X-ray (EDX) spectroscopy clearly indicates the homogeneous distribution of these elements on the perovskite surface, thus indicating a complete coverage of the AF buffer layers on the perovskite. Fig. S9 indicates that the element-content ratio of Pb to I is >3 in all samples, which is consistent with the 10 wt% excess of PbI_2 in the precursor solution. Meanwhile, X-ray diffraction (XRD) measurement (Fig. S10) shows higher crystallinity in all AF-modified perovskite films than the control one. Interestingly, a close view to the (100) peak (in terms of the quasi-cubic lattice of perovskite) of XRD (Fig. 2b) illustrates a shift of this peak toward lower diffraction angle by about 0.1° upon the KF modification which corresponds to an ~0.7% expansion of the lattice constants. Previous studies suggested that such a lattice expansion may result from the occupancy of alkali cations at the interstitial sites [34], which is evidenced by our X-ray photoelectron spectra (XPS) measurements (Fig. S11). These findings indicate that a large number of alkali cations may enter the perovskite lattice at the surface region so that they can reinforce the surface iodide anions via ionic bonding. Besides, ultraviolet-visible absorption and photoluminescence (PL) spectra (Fig. S12) show that the bilateral AF modification has a negligible effect on the bandgap (1.55 eV) of the perovskite samples. Overall, the

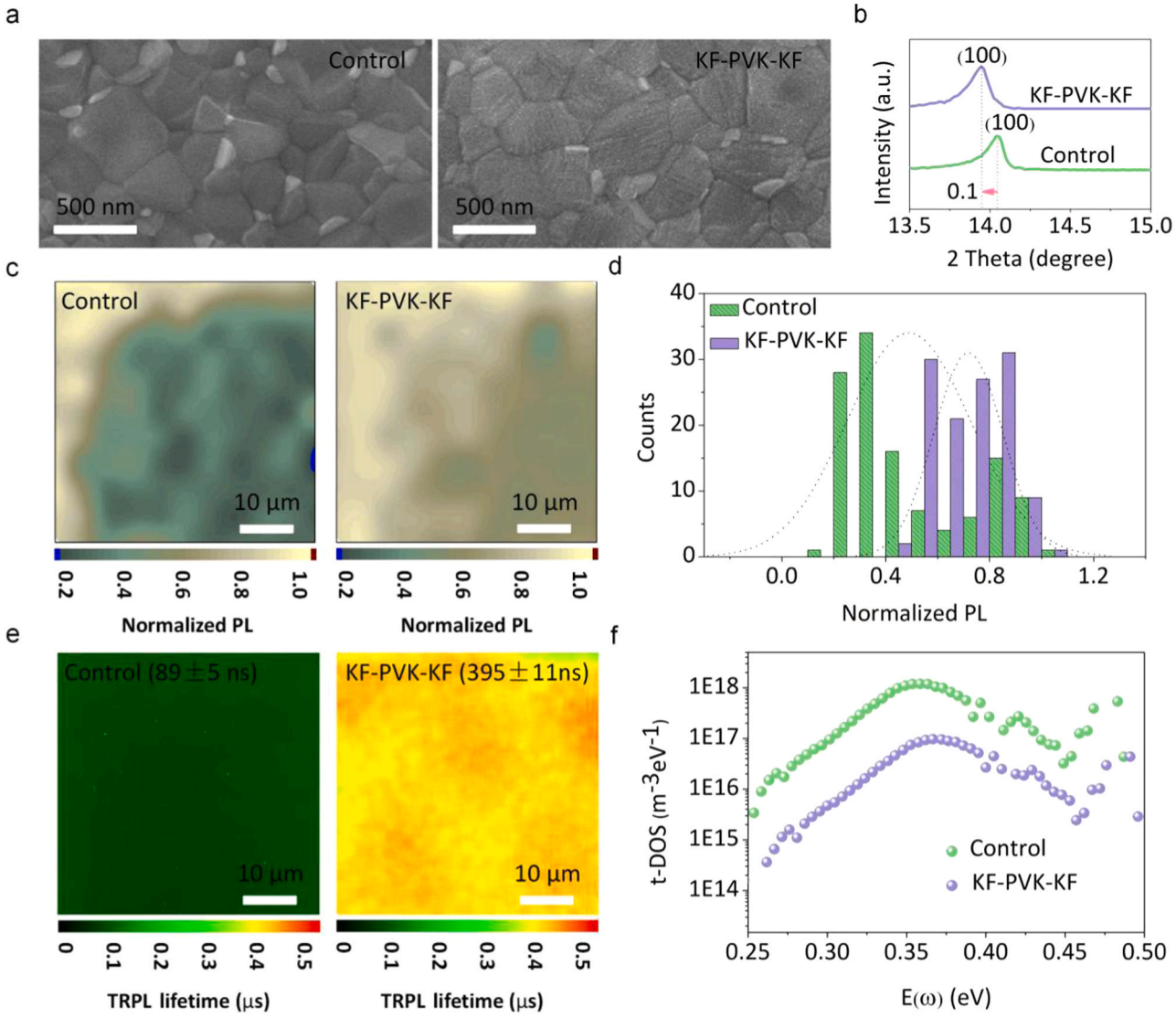

Fig. 2. Materials characterization of perovskite films and trap-state analysis. (a) SEM images of the control and the bilateral KF-interlayers-modified perovskite films. (b) Close view of XRD spectra around the (100) peak. (c) PL mapping of the control and the KF-PVK-KF perovskite film (scanning: 50 μm × 50 μm). (d) Statistic distribution of normalized PL for control and the KF-PVK-KF perovskite film. (e) TRPL mapping for control and the KF-PVK-KF perovskite film (scanning: 50 μm × 50 μm). (f) Trap density of states (t-DOS) for control and AF modified devices.

changes of structural and optical properties of the perovskite bulk upon the incorporation of bilateral AF "walls" are relatively small.

The primary factors that give rise to large V_{OC} loss thus restricting the PCE of PSCs include (a) nonradiative recombination in the bulk of the perovskite absorber, (b) unfavorable energy-level alignment at the perovskite-CTL interfaces, and (c) defect-induced (Shockley-Read-Hall or SRH) recombination at the perovskite surfaces and grain boundaries [39]. The only slight difference in the structural and optical properties between the AF-modified and the control samples, as already alluded to, implies that the obvious improvement of the performance parameters of PSCs upon the KF modification is mainly due to the suppressed SRH recombination at the perovskite surfaces namely its interfaces toward both CTLs. To confirm it, we first carried out PL-mapping and time-resolved PL lifetime (TRPL) mapping measurements that can intuitively describe the spatial distribution of radiative recombination events in both the control and the AF-modified perovskite films on the nanoscale. Consistent with the PL measurements (Fig. S12b), PL-mapping (Fig. 2c) indicates an overall stronger PL of KF-modified perovskite sample than the control. Fig. 2d illustrates the distribution of normalized PL intensities, showing an obviously higher PL homogeneity in the KF-modified perovskite film. The lifetime distribution of TRPL-mapping (Fig. 2e) reveals that the KF-perovskite-KF film is associated with a much longer carrier lifetime (395 ns) than the control (89 ns). TRPL-mapping and its statistics for the other two AF-modified films are given in Fig. S13. The carrier lifetime follows the overall trend: control < LiF-perovskite-LiF < NaF-perovskite-NaF < KF-perovskite-KF, which is consistent with the trend of PSC performance. To summarize, both more pronounced radiative recombination as evidenced by the PL mapping, and the significantly longer charge-carrier lifetime given by the TRPL mapping, support that the introduction of double KF "walls" effectively restricts the nonradiative recombination at the perovskite surfaces and grain boundaries.

Thermal admittance spectroscopy (TAS) was carried out to characterize the local defect density of states (t-DOS). The experiment details and calculations of the t-DOS are given in Supplemental Information [40,41]. As shown in Fig. 2f (and Fig. S14), a density of defect states on the order of 10^{18} m^{-3} was estimated in the control sample. With the bilateral KF modification, the t-DOS is lower by nearly one order of magnitude. We can thus conclude that the introduction of KF ultrathin interlayers can efficiently suppress the formation of surface defects therewith inhibiting interfacial nonradiative recombination.

To further confirm that nonradiative recombination was largely reduced by introducing the bilateral AF "walls" into the system, we carried out a series of measurements on both ITO/HTL/perovskite (HP, as control) and ITO/HTL/interlayer/perovskite/interlayer (HIPI) structure (Fig. 3a), with KF as the interlayer material due to the best performance of the corresponding PSC. Fig. S15 shows the topography of HP and HIPI measured by atomic force microscopy (AFM). Both samples are characterized by a root-mean-square roughness of 15 nm, which agrees with the observation from SEM images that the KF modification

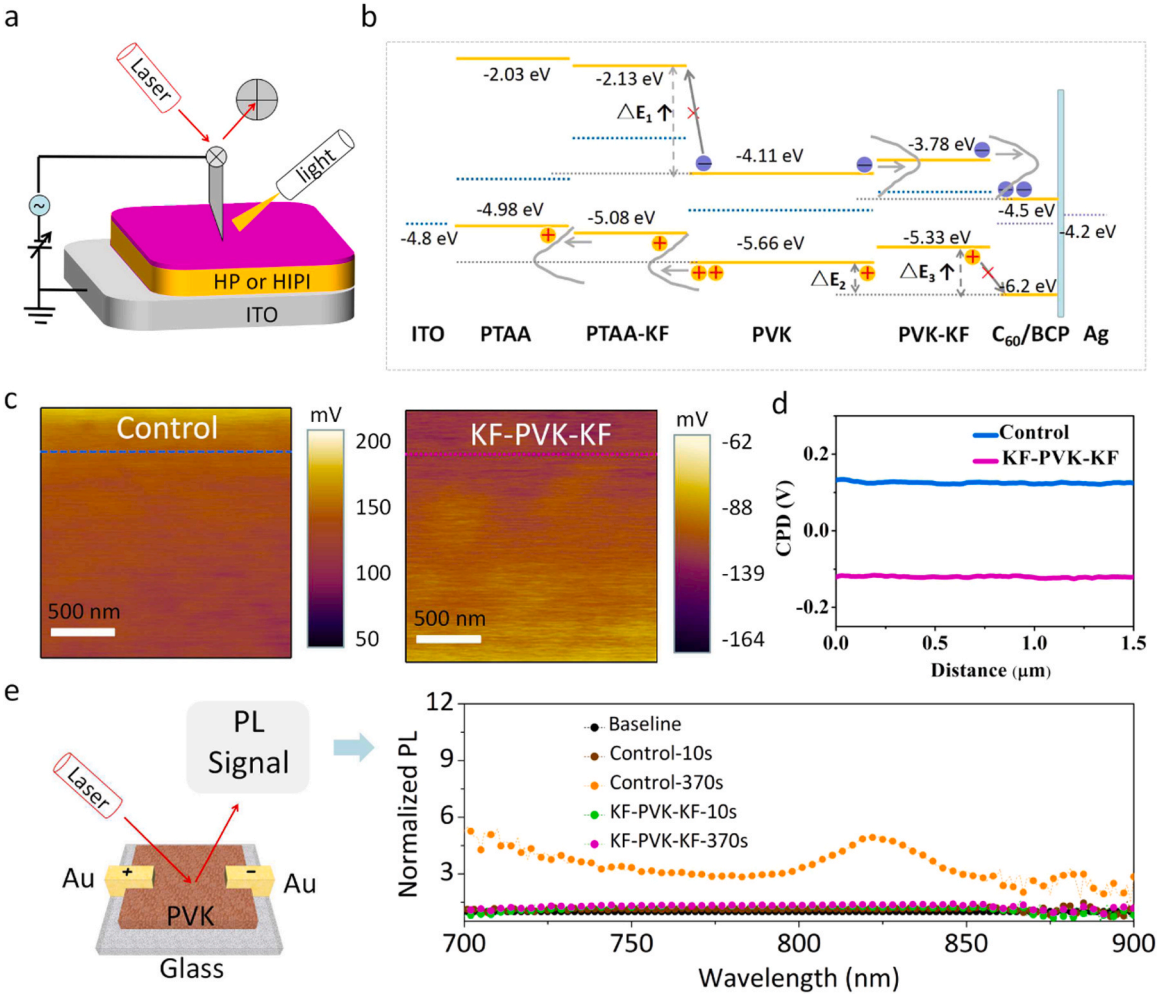

Fig. 3. Charge behaviors at interface. (a) Illustration of the KPFM setup. (b) Energy level alignment of the perovskite solar cells. (c) Surface potential images of PVK/PTAA/ITO (control) and KF-PVK-KF-PTAA-ITO (KF-PVK-KF) sample from KPFM measurements under illumination conditions. (d) 1D line profiles of control and KF-PVK-KF under illumination. (e) Change of normalized PL intensity for control and KF-PVK-KF films under DC 10 V voltage sustaining for 10 s and 370 s.

has not induced drastic changes in the morphology of the perovskite film. Fig. 3c shows the contact potential difference (CPD) distribution of HP and HIPI, respectively, which was measured by Kelvin probe force microscopy (KPFM) under illumination. It is known that the value of CPD is related to the energy barrier of charge extraction at the interface [42,43]. A much lower CPD distribution is observed in HIPI than in HP (Fig. 3d), reflecting a reduced energy barrier. Here the improved efficiency is attributed to the suppressed nonradiative recombination benefitting from the defect-passivating AF buffer layers. The analysis of CPD agrees well with the PL-mapping and TRPL-mapping. The decreased energy barrier is also closely related to the smaller V_{OC} deficit.

We further carefully examined the Photoluminescence quantum efficiency(PLQE) of the perovskite, which serves as an important photophysical analysis to identify a high-quality perovskite films. Generally, defects serve as non-radiative recombination centers to capture the photogenerated charge carriers, thereby dramatically cutting down the PLQE and photovoltaic efficiency in solar cells. Previous work reported that the PLQE was relatively small for perovskite films at low excitation power, but rapidly went up with the increase of excitation power [35]. In Table S6, KF-PVK-KF films on quartz (Quartz/PTAA) exhibited a higher PLQE of ~4.48% (~2.35%), compared with the PVK films on ITO ~2.23% (~1.27%) based on a low excitation power. According to Shockle–Queisser equation, the V_{OC} of the device decreases when the luminescence quantum efficiency of the absorber decreases. Therefore, the higher fluorescence quantum efficiency contributes to the higher V_{oc} for the KF-PVK-KF strategy.

To explore the functions of the inorganic AF interlayers, we first measured the PL with a simplified device structure that consists of two Au electrodes and the control or the KF-perovskite-KF film deposited on glass. With a DC voltage of 10 V, balanced charges of a high concentration were injected into the perovskite film where they recombined and emitted photons. The luminescence intensities of both samples were recorded as a function of injection time. Fig. 3e shows that, at a short injection time (10 s), the luminescence intensities of the control and the KF-sandwiched perovskite films are relatively low and very similar. For a longer injection time (370 s), the control device emitted very much amplified light especially at the wavelengths near the optical band gap, while the intensity of KF-perovskite-KF increased only slightly. This is because the defect-induced states that can trap the injected charge carriers are much fewer in KF-perovskite-KF than in the control sample.

The energy level alignment of PTAA and perovskite before and after modification determined by UPS is shown in Fig. 3b (UPS of PTAA and perovskite with or without KF is shown in Fig. S16a, b). The work function of perovskite is reduced by KF modification, and the corresponding valence band and conduction band are also shifted. Considering the ultra-thin KF, we still use the band gap of perovskite to estimate the value of conduction band. Compared with the control, the valence band of perovskite changed upward after KF modification, which inhibits the accumulation of holes between the perovskite and electron transport layer (C_{60}). However, the conduction band also moved up, but did not change the charge extraction, which may be explained by the charge tunneling theory. The photoelectric characteristics of the device show that the thicker alkali-metal fluoride layers can decrease the short-circuit current density of the devices (Table S1). The main reason is that the inorganic film is too thick, which exceeds the maximum limitation of charge tunneling. Overall, the charge-transport mechanism within the whole PSC device is illustrated by Fig. S16c: the inserted ultrathin AF buffer layers effectively deactivate the unfavorable hole injection from perovskite to ETL (C_{60}/BCP) and the undesired electron injection from perovskite to HTL (PTAA), thus successfully minimizing the nonradiative recombination occurring at both perovskite-ETL and perovskite-HTL interfaces. The desired charge transfer at both interfaces is well facilitated via the charge tunneling theory, so that a reduced V_{OC} loss and thus a high PCE of the photovoltaic device is guaranteed.

For a theoretical insight of how an ultrathin AF protective coating passivates the surface defects of perovskite, we carried out density-functional-theory (DFT) calculations (details given in Supplemental Information) for a series of systems using the all-electron numeric-atom-centered orbital code FHI-aims [44,45]. Considering the relatively large model systems and the computational capacity, we constructed four-layer AF films to mimic the ultrathin interlayers (atomic structures shown in Fig. 4a). Even so, the model systems for the v_I calculations of the LiF-, NaF-, and KF-coated systems contain 1455, 1279, and 1175 atoms, respectively, all above the normal 1000-atom upper limit of traditional DFT calculations.

Two observables are of particular interest: the formation energy of each perovskite-AF complex and the formation energy of v_I defect in each system. The DFT-calculated formation energies of perovskite-LiF, perovskite-NaF, and perovskite-KF are −0.270 eV, −0.109 eV, and −0.313 eV per surface Pb atom, respectively. All values are negative, indicating that the AF films can be spontaneously deposited to the perovskite surface to form stable complexes, thus protecting the perovskite material against possible contact with external particles (such as oxygen, water, and ions from the adjacent functional layers in the device). Note that the atomic geometry of the perovskite surface layer remains flat in all AF-coated structures, meaning that the interaction between the perovskite surface atoms and the AF atoms does not cause noticeable lattice distortion which is very likely harmful to the materials stability. These values do not exhibit a clear trend, possibly because the LiF film has the highest density of atoms thus very likely the highest probability of Li-I and Pb-F bonding at the interface, while the K element has the smallest electronegativity so that the K-I bonds at the interface are stronger than Na-I and Li-I – both can lead to stronger interaction between the perovskite and the AF layer. Another reason might be the largest strain (+1.7%, compared with the −0.55% for LiF and +0.73% for KF) with the NaF in the model system.

The formation energies of (neutral) v_I are 1.90, 2.01, 2.35, and 2.44 eV for the bared (control), LiF-coated, NaF-coated, and KF-coated perovskite surface, respectively (as shown in Fig. 4b). From them we can conclude that all ultrathin AF coatings can suppress the formation of v_I, which are believed to be one of the major sources of nonradiative recombination at the perovskite surfaces and the instability of materials and devices. The effectiveness of AF increases along with LiF < NaF < KF, agreeing well with the results of experimental measurements.

Considering the compactness and stability of the inorganic interlayers as the impenetrable (physically blocking) “walls”, we expect the water and oxygen invasion into the perovskite layer and bidirectional ion migration at the perovskite-CTL interfaces to be largely prevented. To this end, we carried out time-of-flight secondary ion mass spectroscopy (ToF-SIMS) to probe the depth profiles of the atomic species within the sample (Fig. 4d). The much shallower diffusion of Ag^+ into the perovskite layer, and the obviously reduced I^--distribution in PTAA and especially C_{60}, evidence the physical-blocking functionality of the AF buffer layers. With the induced huge energy barrier for small particles to penetrate, it is also natural to expect that the AF buffer layers can well protect the perovskite surface against the interaction with environmental small molecules such as oxygen and water, which easily leads to material degradation. The binding energies of carbon from XPS results (Fig. 4c) show C and C-N peaks located at 284.6 eV and 286.1 eV for all the perovskite samples. For KF modification, an additional peak at a binding energy of 292.9 eV emerges signifying the K^+ cations. Notably, the control film exhibits a strong signal at 288.1 eV which is attributed to the C═O bonding [46], indicating a prevalent interaction with oxygen. As AF varies from LiF to NaF and KF, this undesired C═O peak gradually diminishes and finally almost disappears.

We also investigated the potential of applying the inverted planar perovskite photovoltaic devices with inorganic bilateral buffer layers in indoor light-harvesting (schematic diagram shown in Fig. 5a). As already reported, perovskite-based devices perform excellently under dim-light condition as a result of the large component-flexibility of

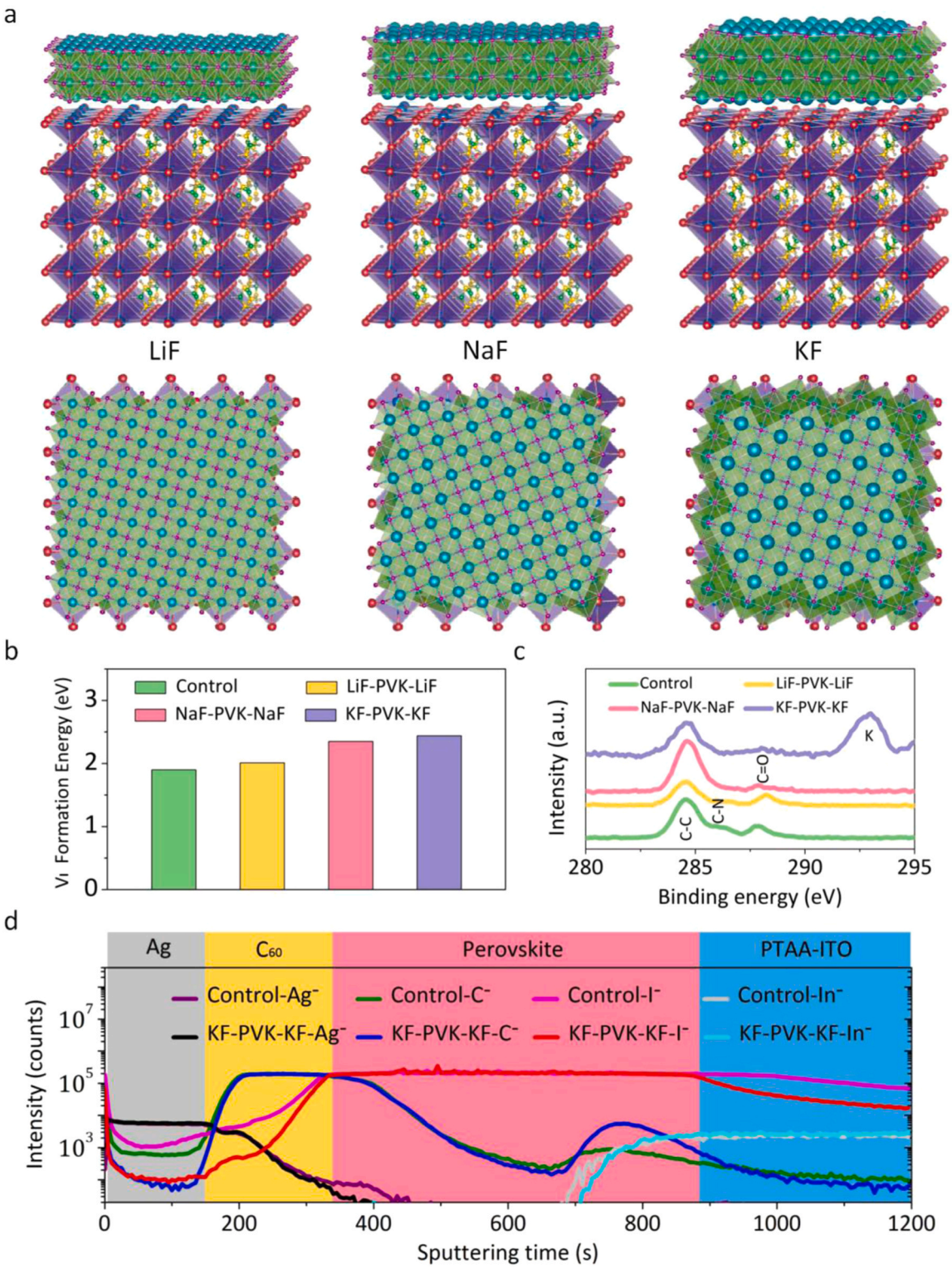

Fig. 4. Mechanism of the chemical anchoring and physical blocking. (a) DFT-optimized structures of $FAPbI_3$-AF complexes (left, middle, and right for A = Li, Na, and K, respectively; C, N, H, Pb, I, A, and F in green, yellow, gray, blue, red, turquoise, and purple, respectively). (b) Formation energy of surface v_I defects calculated with DFT. (c) XPS spectra of the perovskite films without and with AF modification, showing the binding energy of C 1s bound to different elements (plus the K $2p_{3/2}$ of the KF-PVK-KF sample). (d) ToF-SIMS elemental depth profiles of control and KF-PVK-KF aged for 300 h of illumination under N_2 atmosphere.

materials and therewith the tunable bandgap (Table S7) [9]. Fig. 5b shows the illumination spectrum and chromaticity coordinate of the white LED. This spectrum corresponds to a maximal PCE (detailed balance limit) of 53% associated with a bandgap of 1.9 eV. Fig. 5c shows the indoor *J–V* curves of the devices with and without KF modification under a white LED source, with the parameters presented in Table S8. Under standard LED low illumination (1000 lux, color temperature = 5900 K, power density = 292 μW/cm^2), a PCE of 24.9% (J_{SC} = 126 μA/cm^2, V_{OC} = 0.81 V, FF = 71.2%) was achieved by the control device, while an outstanding performance of 35.7% PCE was obtained

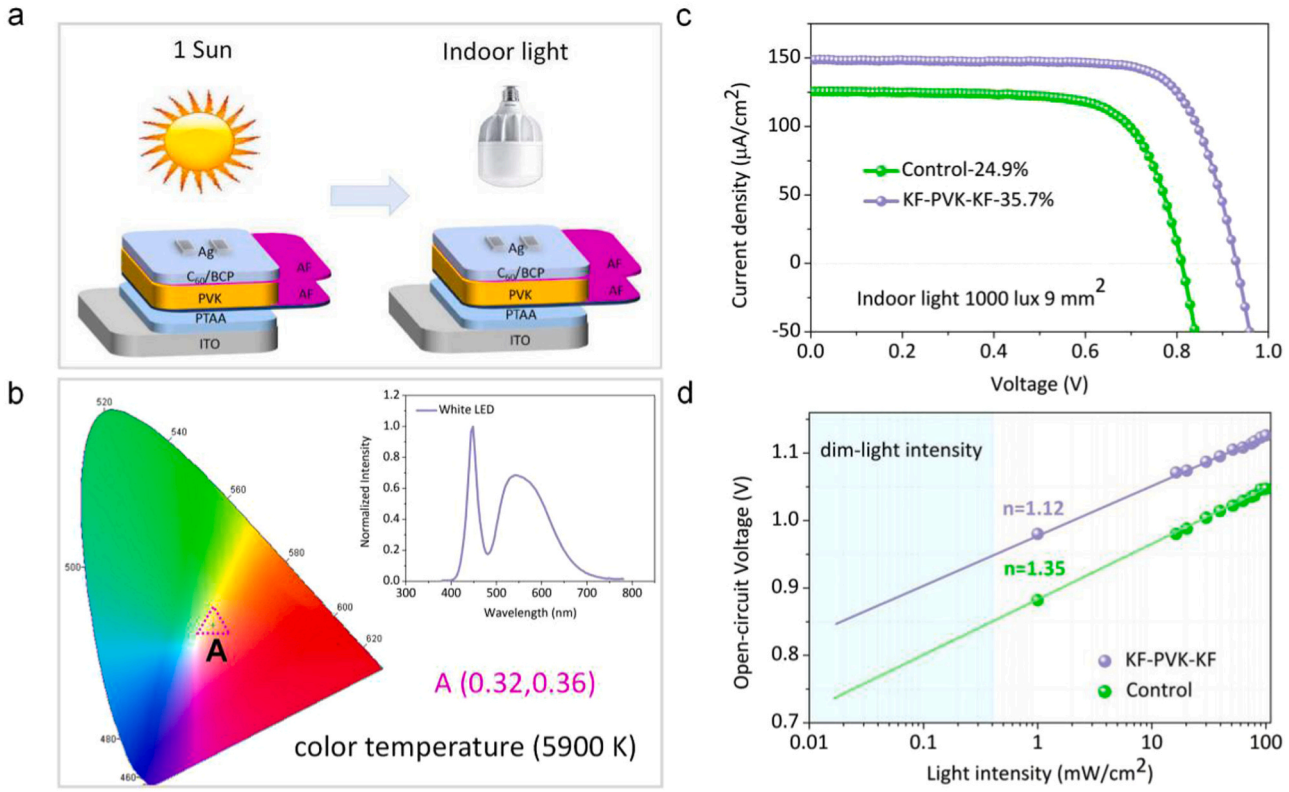

Fig. 5. Performance of indoor-photovoltaic devices. (a) Schematic diagram of devices for control and KF-PVK-KF under one sun and indoor light. (b) Illumination spectra and chromaticity coordinate of white LED. (c) *J-V* characteristics of a 9 mm^2 device at 1000 lux. (d) V_{OC} measured at different light intensity under AM 1.5 G with extrapolation to the dim-light-intensity region.

with the KF-modified device (J_{SC} = 148 μA/cm^2, V_{OC} = 0.93 V, FF = 75.7%). The performance improvement in indoor-photovoltaic applications upon the incorporation of KF interlayers is thus much more significant than in solar-light harvesting. We expect an even better performance of inverted planar perovskite devices with this inorganic bilateral strategy for indoor-light photovoltaics, for example, providing that the bandgap is tuned closer to the optimal value with proper materials engineering.

In Fig. 5d, the relationship between V_{OC} and the light intensity of different devices (solar spectrum) was measured, and the diode ideality factor n ($1 < n < 2$) was calculated using the following equation:

$$V_{OC} \sim \frac{nKT}{e} \ln\left(\frac{I_{ph}}{I_0}\right) \quad (1)$$

where k is the Boltzmann constant, T is the temperature, e is the elementary charge, I_{ph} is the photocurrent, and I_0 is the saturation current of the diode. By fitting the data, the ideality factors n of the device are 1.35 and 1.12 for the control and the KF-modified devices, respectively. A larger n value corresponds to a more severe trap-assisted SRH recombination. Therefore these results signify a successful suppression of defect-induced trap states with the help of the bilateral ultrathin KF interlayers.

3. Conclusion

In summary, we have proposed an inorganic strategy of surface engineering to improve the efficiency and stability of PSCs. By coating ultrathin KF films at the surfaces of the triple-cation perovskite active layer with a nearly complete coverage, that is, modifying both perovskite-ETL and perovskite-HTL interfaces, the formation of defects at the perovskite surfaces and grain boundaries as well as the bidirectional ion migration at the interfaces were substantially suppressed as evidenced by both experimental and theoretical analysis. As a result, the defect-induced nonradiative recombination was significantly reduced thus leading to the more effective interfacial charge extraction and the less material degradation. With the optimized devices we obtained a PCE of 22.02% which is among the best records for inverted planar PSCs. The unencapsulated devices exhibit exceptional operational stability (500 h, ISOS-L-2) and thermal stability (1000 h, ISOS-D-2). A remarkable PCE of 35.7% was achieved under a standard white-light LED source with these devices, which also belongs to the best records of indoor photovoltaics to-date and shows a promising future in indoor-light harvesting. Our approach thus offers a new solution to the critical problem of today's perovskite optoelectronic community, and opens up space for further advancement of perovskite-based photovoltaic techniques toward high efficiency and high stability in both outdoor and indoor applications.

CRediT authorship contribution Statement

Jie Xu and **Jun Xi** conceived and designed the experiments, including fabrication and analysis of the films and devices. **Jinbo Chen** contributed to absorption spectra measurement and analysis. **Jie Xu** wrote the first version of the manuscript. **Jun Xi** contributed to the modification of manuscript. All authors discussed the results and contributed to the final version of the paper. **Hua Dong**, **Jingrui Li** and **Zhaoxin Wu** supervised the project.

Declaration of Competing Interest

The authors declare that they have no known competing financial interests or personal relationships that could have appeared to influence the work reported in this paper.

Acknowledgments

This work is financially supported by the National Natural Science Foundation of China (Grant Nos. 61604121, 61935016). China Postdoctoral Science Foundation (Grant No. 2019M663717, 2020T130502), Scientific Research Plan Projects of Shaanxi Education Department (Grant No. 17JK0700), Natural Science Basic Research Plan in Shaanxi Province of China (Grant No. 2019JQ-119), The authors thank Chunyan Lu and Yanyan Wang at Ningbo University for her help in using KPFM. The authors thank Dr. Yuansheng Sun and Dr. Dongsheng Wu at ISS, Inc. for his help of FastFLIM records. We also thank Dr. Liu at the Instrumental Analysis Center of Xi'an Jiaotong University for her assistance with XPS/UPS analysis. This work is also supported by Xi'an Jiaotong University's HPC Platform.

Appendix A. Supporting information

Supplementary data associated with this article can be found in the online version at doi:10.1016/j.nanoen.2021.106286.

References

[1] J. Feng, B. Xiao, Crystal structures, optical properties, and effective mass tensors of CH3NH3PbX3 (X = I and Br) phases predicted from HSE06, J. Phys. Chem. Lett. 5 (2014) 1278–1282.
[2] S. Stranks, G. Eperon, G. Grancini, C. Menelaou, M. Alcocer, T. Leijtens, L. Herz, A. Petrozza, H. Snaith, Electron-hole diffusion lengths exceeding 1 micrometer in an organometal trihalide perovskite absorber, Science 342 (2013) 341–344.
[3] E. Edri, S. Kirmayer, S. Mukhopadhyay, K. Gartsman, G. Hodes, D. Cahen, Elucidating the charge carrier separation and working mechanism of CH3NH3PbI (3-x)Cl(x) perovskite solar cells, Nat. Commun. 5 (2014) 3461.
[4] J. Noh, S. Im, J. Heo, T. Mandal, S. Seok, Chemical management for colorful, efficient, and stable inorganic-organic hybrid nanostructured solar cells, Nano Lett. 13 (2013) 1764–1769.
[5] S. Wolf, J. Holovsky, S. Moon, P. Löper, B. Niesen, M. Ledinsky, F. Haug, J. Yum, C. Ballif, Organometallic halide perovskites: sharp optical absorption edge and its relation to photovoltaic performance, J. Phys. Chem. Lett. 5 (2014) 1035–1039.
[6] G. Xing, N. Mathews, S. Sun, S.S. Lim, Y.M. Lam, M. Grätzel, S. Mhaisalka, T. C. Sum, Long-range balanced electron- and hole-transport lengths in organic-inorganic CH3NH3PbI3, Science 342 (2013) 344–347.
[7] Q. Dong, Y. Fang, Y. Shao, P. Mulligan, J. Qiu, L. Cao, J. Huang, Electron-hole diffusion lengths > 175 μm in solution-grown CH3NH3PbI3 single crystals, Science 347 (2015) 967–970.
[8] NREL, "Best Research-Cell Efficiencies", ⟨https://www.nrel.gov/pv/assets/pdfs/best-research-cell-efficiencies.20200925.pdf⟩.
[9] R. Cheng, C. Chung, H. Zhang, F. Liu, W. Wang, Z. Zhou, S. Wang, A. Djurišić, S. Feng, Tailoring triple-anion perovskite material for indoor light harvesting with restrained halide segregation and record high efficiency beyond, Adv. Energy Mater. 9 (2019), 1901980.
[10] W. Shockley, H. Queisser, Detailed balance limit of efficiency of p-n junction solar cells, J. Appl. Phys. 32 (1961) 510–519.
[11] M. Stolterfoht1, C. Wolff, J. Márquez, S. Zhang, C. Hages, D. Rothhardt, S. Albrecht, P. Burn, P. Meredith, T. Unold, D. Neher, Visualization and suppression of interfacial recombination for high-efficiency large-area pin perovskite solar cells, Nat. Energy 3 (2018) 847–854.
[12] F. Li, X. Deng, F. Qi, Z. Li, D. Liu, D. Shen, M. Qin, S. Wu, F. Lin, S. Jang, J. Zhang, X. Lu, D. Lei, C. Lee, Z. Zhu, A. Jen, Regulating surface termination for efficient inverted perovskite solar cells with greater than 23% efficiency, J. Am. Chem. Soc. 142 (2020) 20134–20142.
[13] J. Xi, C. Piao, J. Byeon, J. Yoon, Z. Wu, M. Choi, Rational core–shell design of open air low temperature in situ processable CsPbI3Quasi-nanocrystals for stabilized p-i-n solar cells, Adv. Energy Mater. 9 (2019), 1901787.
[14] J. Yoon, H. Sung, G. Lee, W. Cho, N. Ahn, H. Jung, M. Choi, Superflexible, high-efficiency perovskite solar cells utilizing graphene electrodes: towards future foldable power sources, Energy Environ. Sci. 10 (2017) 337–345.
[15] A.G. Boldyreva, I.S. Zhidkov, S. Tsarev, A.F. Akbulatov, M.M. Tepliakova, Y. S. Fedotov, S.I. Bredikhin, E.Y. Postnova, S.Y. Luchkin, E.Z. Kurmaev, K. J. Stevenson, P.A. Troshin, Unraveling the impact of hole transport materials on photostability of perovskite films and p-i-n solar cells, ACS Appl. Mater. Interfaces 12 (2020) 19161–19173.
[16] M. Stolterfoht, P. Caprioglio, C. Wolff, J. Marqúez, J. Nordmann, S. Zhang, D. Rothhardt, U. Hörmann, Y. Amir, A. Redinger, L. Kegelmann, F. Zu, S. Albrecht, N. Koch, T. Kirchartz, M. Saliba, T. Unold, D. Neher, The impact of energy alignment and interfacial recombination on the internal and external open-circuit voltage of perovskite solar cells, Energy Environ. Sci. 12 (2019) 2778–2788.
[17] D. Shohl, Y. Zhou, N. Padture, D. Mitzi, Synthetic approaches for halide perovskite thin films, Chem. Rev. 119 (2019) 3193–3295.
[18] X.X. Liu, Z.G. Yu, T. Wang, X.X. Chiu, F. Lin, H. Gong, L.M. Ding, Y.H. Cheng, Full defects passivation enables 21% efficiency perovskite solar cells operating in air, Adv. Energy Mater. 10 (2020), 2001958.
[19] Y.M. Li, H.X. Wu, W.J. Qi, X. Zhou, J.L. Li, J. Cheng, Y. Zhao, Y.L. Li, X.D. Zhang, Passivation of defects in perovskite solar cell: from a chemistry point of view, Nano Energy 77 (2020), 105237.
[20] F. Gao, Y. Zhao, X.W. Zhang, J.B. You, Recent progresses on defect passivation toward efficient perovskite solar cells, Adv. Energy Mater. 10 (2020), 1902650.
[21] E. Aydin, M.D. Bastiani, S.D. Wolf, Defect and contact passivation for perovskite solar cells, Adv. Mater. 31 (2019), 1900428.
[22] N. Ahn, K. Kwak, M. Jang, H. Yoon, B. Lee, J. Lee, P. Pikhitsa, J. Byun, M. Choi, Trapped charge-driven degradation of perovskite solar cells, Nat. Commun. 7 (2016) 13422.
[23] J. Byeon, J. Kim, J. Kim, G. Lee, K. Bang, N. Ahn, M. Choi, Charge transport layer-dependent electronic band bending in perovskite solar cells and its correlation to light-induced device degradation, ACS Energy Lett. 5 (2020) 2580–2589.
[24] C. Wolff, L. Canil, C. Rehermann, N. Linh, F. Zu, M. Ralaiarisoa, P. Caprioglio, L. Fiedler, M. Stolterfoht, S. Kogikoski, J. Bald, N. Koch, E. Unger, T. Dittrich, A. Abate, D. Neher, Perfluorinated self-assembled monolayers enhance the stability and efficiency of inverted perovskite solar cells, ACS Nano 14 (2020) 1445–1456.
[25] S. Wu, J. Zhang, Z. Li, D. Liu, M. Qin, S. Cheung, X. Lu, D. Lei, S. So, Z. Zhu, A. Jen, Modulation of defects and interfaces through alkylammonium interlayer for efficient inverted perovskite solar cells, Joule 4 (2020) 1248–1262.
[26] A. Krishna, S. Gottis, M. Nazeeruddin, F. Sauvage, Mixed dimensional 2D/3D hybrid perovskite absorbers: the future of perovskite solar cells, Adv. Funct. Mater. 29 (2018), 1806482.
[27] S. Wang, Z. Zhang, Z. Tang, C. Su, W. Huang, Y. Li, G. Xing, Polymer strategies for high-efficiency and stable perovskite solar cells, Nano Energy 82 (2021), 105712.
[28] M. Kim, S. Motti, R. Sorrentinoab, A. Petrozza, Enhanced solar cell stability by hygroscopic polymer passivation of metal halide perovskite thin film, Energy Environ. Sci. 11 (2018) 2609–2619.
[29] H. Dong, Y. Li, S. Wang, W. Li, N. Li, X. Guo, L. Wang, Interface engineering of perovskite solar cells with PEO for improved performance, J. Mater. Chem. A 3 (2015) 9999–10004.
[30] Z. Wu, Z. Liu, Z. Hu, Z. Hawash, L. Qiu, Y. Jiang, L. Ono, Y. Qi, Highly efficient and stable perovskite solar cells via modification of energy levels at the perovskite/carbon electrode interface, Adv. Mater. 31 (2019), 1804284.
[31] M. Abdi-Jalebi, Z. Andaji-Garmaroudi, S. Cacovich, C. Stavrakas, B. Philippe, J. Richter, M. Alsari, E. Booker, E. Hutter, A. Pearson, S. Lilliu, T. Savenije, H. Rensmo, G. Divitini, C. Ducati, R. Friend, S. Stranks, Maximizing and stabilizing luminescence from halide perovskites with potassium passivation, Nature 555 (2018) 497–501.
[32] Z. Tang, T. Bessho, F. Awai, T. Kinoshita, M. Maitani, R. Jono, T. Murakami, H. Wang, T. Kubo, S. Uchida, H. Segawa, Hysteresis-free perovskite solar cells made of potassium-doped organometal halide perovskite, Sci. Rep. 7 (2017) 12183.
[33] D. Son, S. Kim, J. Seo, S. Lee, H. Shin, D. Lee, N. Park, Universal approach toward hysteresis-free perovskite solar cell via defect engineering, J. Am. Chem. Soc. 140 (2018) 1358–1364.
[34] J. Cao, S. Tao, P. Bobbert, C. Wong, N. Zhao, Interstitial occupancy by extrinsic alkali cations in perovskites and its impact on ion migration, Adv. Mater. 30 (2018), 1707350.
[35] Y. Chen, N. Li, L. Wang, L. Li, Z. Xu, H. Jiao, P. Liu, C. Zhu, H. Zai, M. Sun, W. Zou, S. Zhang, G. Xing, X. Liu, J. Wang, D. Li, B. Huang, Q. Chen, H. Zhou, Impacts of alkaline on the defects property and crystallization kinetics in perovskite solar cells, Nat. Commun. 10 (2019) 1112.
[36] L. Zhang, F. Yuan, J. Xi, B. Jiao, H. Dong, J. Li, Z. Wu, Suppressing ion migration enables stable perovskite light-emitting diodes with all-inorganic strategy, Adv. Funct. Mater. 30 (2020), 2001834.
[37] L. Xu, M. Qian, C. Zhang, W. Lv, J. Jin, J. Zhang, C. Zheng, M. Li, R. Chen, W. Huang, In situ construction of gradient heterojunction using organic VOx precursor for efficient and stable inverted perovskite solar cells, Nano Energy 67 (2020), 104244.
[38] C. Bi, Q. Wang, Y. Shao, Y. Yuan, Z. Xiao, J. Huang, Non-wetting surface-driven high-aspect-ratio crystalline grain growth for efficient hybrid perovskite solar cells, Nat. Commun. 6 (2015) 7747.
[39] C. Wolff, P. Caprioglio, M. Stolterfoht, D. Neher, Nonradiative recombination in perovskite solar cells: the role of interfaces, Adv. Mater. 31 (2019), 1902762.
[40] Y. Shao, Y. Yuan, J. Huang, Correlation of energy disorder and open-circuit voltage in hybrid perovskite solar cells, Nat. Energy 1 (2016) 15001.
[41] N. Li, S. Tao, Y. Chen, X. Niu, C. Onwudinanti, C. Hu, Z. Qiu, Z. Xu, G. Zheng, L. Wang, Y. Zhang, L. Li, H. Liu, Y. Lun, J. Hong, X. Wang, Y. Liu, H. Xie, Y. Gao, Y. Bai, S. Yang, G. Brocks, Q. Chen, H. Zhou, Cation and anion immobilization through chemical bonding enhancement with fluorides for stable halide perovskite solar cells, Nat. Energy 4 (2019) 408–415.
[42] C.P. Jiang, P.P. Zhang, Crystalline orientation dependent photoresponse and heterogeneous behaviors of grain boundaries in perovskite solar cells, J. Appl. Phys. 123 (2018), 083105.
[43] J.S. Yun, A. Ho-Baillie, S. Huang, S.H. Woo, Y. Heo, J. Seidel, F. Huang, Y.B. Cheng, M.A. Green, Benefit of grain boundaries in organic-inorganic halide planar perovskite solar cells, J. Phys. Chem. Lett. 6 (2015) 875–880.

[44] V. Gehrke, F. Hanke, P. Havu, V. Havu, X. Ren, K. Reuter, M. Scheffler, Ab initio molecular simulations with numeric atom-centered orbitals, Comput. Phys. Commun. 180 (2009) 2175–2196.
[45] V. Havu, V. Blum, P. Havu, M. Scheffler, Efficient integration for all-electron electronic structure calculation using numeric basis functions, J. Comput. Phys. 228 (2009) 8367–8379.
[46] Q. Jiang, Y. Zhao, X.W. Zhang, X.L. Yang, Y. Chen, Z. Chu, Q.F. Ye, X.X. Li, Z. Yin, J.B. You, Surface passivation of perovskite film for efficient solar cells, Nat. Photon. 13 (2019) 460–466.